



1 **Testing ground based observations of wave activity in the (lower and upper) atmosphere**  
2 **as possible (complementary) indicators of streamer events**

3 **Michal Kozubek<sup>1</sup>, Lisa Kuchelbacher<sup>2</sup>, Jaroslav Chum<sup>1</sup>, Tereza Sindelarova<sup>1</sup>, Franziska**  
4 **Trinkl<sup>2, a</sup>, Katerina Podolska<sup>1</sup>**

5 <sup>1</sup>Institute of Atmospheric Physics CAS, Bocni II 1401, Prague, 14100, Czech Republic

6 <sup>2</sup> Earth Observation Center, Deutsches Zentrum für Luft- und Raumfahrt, 82234 Weßling,  
7 Germany

8 <sup>a</sup> now at Karlsruhe Institute of Technology (KIT), Institute of Meteorology and Climate  
9 Research, Karlsruhe, Germany

10 **Correspondence: Michal Kozubek, [kom@ufa.cas.cz](mailto:kom@ufa.cas.cz)**

11 **Keywords:** gravity waves, streamer events, infrasound, Doppler measurements

12

13 **Abstract:** For a better understanding of atmospheric dynamics, it is very important to know  
14 the general condition (dynamics and chemistry) of the atmosphere. Planetary waves (PWs) are  
15 global scale waves, which are well-known as main drivers of the large-scale weather patterns  
16 in mid-latitudes on time scales from several days up to weeks in the troposphere. When PWs  
17 break, they often cut pressure cells off the jet stream. A specific example are so-called  
18 streamer events, which occur predominantly in the lower stratosphere at mid- and high-  
19 latitudes. For streamer events we check, whether there are any changes of gravity wave (GW)  
20 or infrasound characteristics related to these events in ionospheric and surface measurements  
21 (continuous Doppler soundings, array of microbarometers) in the Czech Republic. First order  
22 signatures of streamer events were not identified in infrasound data at stations WBCI and  
23 PVCI. Supplementary ground-based measurements of GW using the WBCI array in the  
24 troposphere showed that GW propagation azimuths were more random during streamer and  
25 streamer-like events compared to those observed during calm conditions. GW propagation  
26 characteristics observed in the ionosphere by continuous Doppler soundings during streamer  
27 events did not differ from those expected for the given time period.

28

29

30



31

## 32 **1) Introduction**

33 For a better comprehension of climate change it is fundamentally important, how well we  
34 understand the climate system in general, and the dynamics of the atmosphere in particular.  
35 The dynamic processes relevant in this context in the atmosphere take place over a  
36 comparatively wide range of scales in space and time. They include in particular both,  
37 planetary and gravity waves. Planetary waves are the main drivers of the extratropical  
38 circulation. When they break they lead to an irreversible exchange of air masses between the  
39 equatorial and polar region due to an amplification of their amplitudes (e.g. McIntyre &  
40 Palmer, 1983; Polvani & Plumb, 1992). In the upper troposphere / lower stratosphere ozone  
41 can be used as a tracer for these large-scale motions, as it has a comparatively long life-time.  
42 When planetary waves break tropical air masses of low ozone concentration are mixed  
43 poleward into the surrounding atmosphere of the mid and higher latitudes (e.g. Leovy et al.,  
44 1985). Streamer events do not have a unique definition in literature, which makes them  
45 difficult to detect objectively. As those streamer events originate by planetary wave dynamics,  
46 the spatio-temporal characteristics are closely linked. They persist for days to weeks and  
47 extend over a region of several 1000 km. Often smaller scale air masses detach from these  
48 streamers and are irreversibly mixed into the higher latitudes. It is found that streamers mainly  
49 occur at the transition zone from the Northern Atlantic to Europe and also, but less often,  
50 from the Northern Pacific to Northern America (e.g. Eyring et al., 2002; James, 1998) which is  
51 why we will focus on the Northern Atlantic / European transition region. During a streamer  
52 event the wind field changes rather strong over a comparatively small distance. Since a  
53 streamer event shows a strong wind shear at its flanks, it is expected that it excites GW (e.g.  
54 Kramer et al., 2015 and 2016 or Peters et al., 2003). Therefore, our focus will be on GW  
55 periods.

56 It is well-known that enhanced wind gradients or anticyclones can lead to the excitation of  
57 gravity waves (GW) in the atmosphere (e.g. Pramitha et al., 2015; Kai et al., 2010; Kramer et  
58 al., 2015, 2016 and Gerlach et al., 2003). GW have typical vertical wavelengths from a few  
59 100 m to several kilometres (Wüst & Bittner, 2006), and horizontal wavelengths over tens km  
60 (Wüst et al., 2018), and longer (Rauthe et al., 2006); their fluctuations in the upper  
61 troposphere / lower stratosphere typically show amplitudes of 5–10 m/s at maximum (e.g.,  
62 Kramer et al., 2015). Those waves transport energy and momentum horizontally and  
63 vertically through the atmosphere and deposit them especially in the mesosphere but also



64 above and below this height region. The propagation of GWs is strongly dependent on the  
65 wind conditions in the stratosphere since the wind field of the middle atmosphere (10–100  
66 km) reaches its maximum there. That is why monitoring waves in upper parts of the  
67 atmosphere, e.g. based on Doppler observations in the ionosphere, can provide us additional  
68 information about stratospheric conditions (for details see Fritts and Alexander, 2003).

69 Using pressure recordings at a microbarograph array, GWs and infrasound at the ground can  
70 be observed. Ground based observations of GWs at a large aperture microbarograph array are  
71 utilized in the present study as an independent data source for the analysis of GW activity  
72 during streamer events. Infrasound propagation is influenced by wind and temperature fields  
73 in the atmosphere. Three regions play an important role in long-distance infrasound  
74 propagation: (1) the lower thermosphere; (2) the stratosphere; (3) the jet stream near the  
75 tropopause and inversion layers in the troposphere (Evers and Haak, 2010). Infrasound  
76 observed at the ground and emitted by distant sources mostly propagates in the stratospheric  
77 waveguide (Ceranna et al., 2019). A number of case studies have proved that stratospheric  
78 dynamics can be deduced from microbarograph measurements at the ground (Assink et al.,  
79 2014; Blixt et al., 2019; Evers and Siegmund, 2009; Evers et al., 2012; Garcès et al., 2004; Le  
80 Pichon and Blanc, 2005; Le Pichon et al., 2006 and 2009; Smets and Evers, 2014). Streamer  
81 events are significant transient disturbances to circulation patterns in the tropopause/lower  
82 stratosphere region; modifications of the stratospheric waveguide can therefore be expected.  
83 A feasibility study on utilisation of ground infrasound measurements in research of streamer  
84 events will be performed using data from two infrasound stations in the Czech Republic. Its  
85 aim will be to identify possible first order phenomena in infrasound detections related to the  
86 streamers – significant deviations in infrasound arrival parameters with focus on the azimuth  
87 of signal arrival, signal amplitude and frequency fluctuations. If an occurrence of such  
88 phenomena was proved during streamer events and if attributes of the phenomena were  
89 generally applicable, notification of a streamer event could be based on a routine operational  
90 evaluation of infrasound detections as such (without using complementary datasets) and  
91 ground based infrasound measurements could serve as a quick indicator of streamers.

92 Our study will focus on possible utilization Doppler sounding and microbarographs for  
93 description and analysis of GW behaviour and propagation in the stratosphere.



94 The structure of the paper is as follow: After introduction the description of the used dataset  
95 and method can be found in the second section. Then we describe our results and in the last  
96 section we discuss the possible connection to previous studies.

97

## 98 **2) Data and methods**

99 The data basis of the selection of the streamer events are global maps of total ozone column  
100 measurements (TO3) which are available as a service by DLR (<https://atmos.eoc.dlr.de/>). TO3  
101 is retrieved by the Tropospheric Monitoring Instrument (TROPOMI) on the Sentinel 5  
102 Precursor (S5P) mission. Whenever no data by TROPOMI/S5P is available, TO3  
103 measurements of the Global Ozone Monitoring Experiment-2 (GOME-2) on the Metop series  
104 of satellites is considered. Both instruments are nadir-viewing on a near-polar sun-  
105 synchronous orbit. TROPOMI/S5P was launched in 2017 and has a spatial resolution of 7x7  
106 km<sup>2</sup> with a daily global coverage and a repeat cycle of 17 days (Veefkind et al. 2012). Details  
107 on TO3 by TROPOMI/S5P are given by Spurr et al. (2022). The TO3 retrieval is based on the  
108 processor of the previous GOME instrument: GOME-2 on Metop-AB was launched in 2006.  
109 It has a spatial resolution of 80x40 km<sup>2</sup> and almost a daily global coverage with a repeat cycle  
110 of 29 days. See Munro et al. 2006 and Munro et al. 2016 for an overview of the instrument  
111 and data processing. Details of the GOME-2 retrieval algorithm can be found in Loyola et al  
112 (2011).

113 Streamer events are selected manually for this study, as no distinct definition exists. As  
114 planetary waves are permanently disturbing the atmospheric dynamic, especially smaller scale  
115 streamers can be observed almost every day and the differentiation between streamer events  
116 and calm events becomes subjective. We therefore focus on few events which are  
117 comparatively strong in their evolution from our perspective. Moreover, we focus on streamer  
118 events above the Northern Atlantic. Whenever another streamer event occurs at the same time  
119 at another latitudinal region with comparable spatiotemporal extent, we do not consider this  
120 date as a streamer event. We assume that the effects of the streamer superimpose and a  
121 distinct backtrack to the streamer over the Northern Atlantic will not be possible. This means,  
122 that the analysis of the streamer events can be blurred to some extent.

123 We consider dates from January 2020 to April 2021. In general, planetary waves drive the  
124 Brewer Dobson Circulation in the stratosphere during winter and ozone-poor airmasses are



125 transported northward. Streamer events are therefore detected between September and March.  
126 The streamer events are distinguished if they have a large spatial size, high intensity (low  
127 TO<sub>3</sub> concentration) and if air masses are irreversibly mixed into the surrounding atmosphere.  
128 All the selected events persist for several days, but no longer than 10 days. The streamer  
129 events given in table 1 (left) are selected manually, by the given criterions.

130 To evaluate weather streamer events effect the smaller-scale atmospheric dynamics, calm  
131 events are identified as well by subjective criterions. These events serve as a reference to  
132 streamer events, as large-scale dynamics are hardly visible in the TO<sub>3</sub>. The events are  
133 selected when the ozone concentration shows a strong meridional gradient from the equator to  
134 polar region on the Northern Hemisphere with almost no longitudinal variation. The examples  
135 of calm atmospheric dynamics are listed in table 1 (right).

136

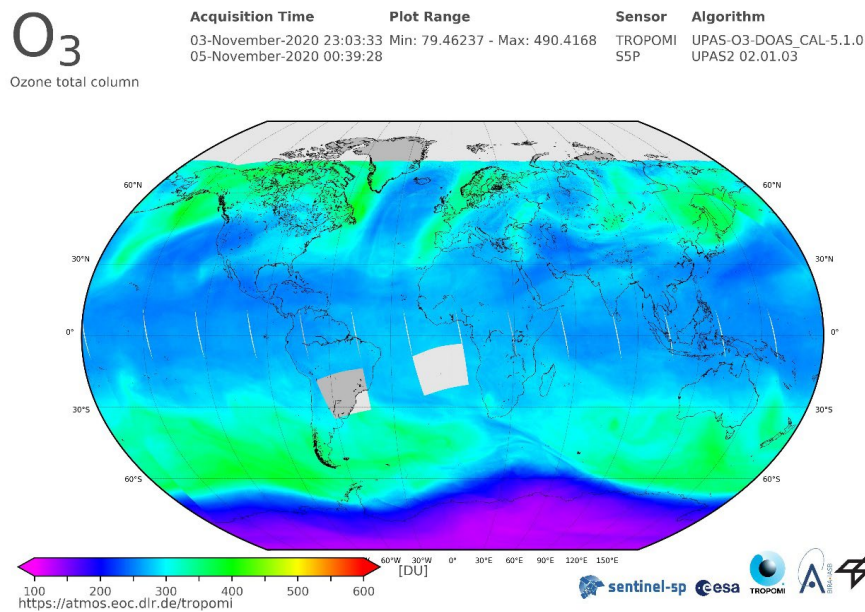
Streamer events		Calm periods	
From	To	From	To
06.02.2020	10.02.2020	02.03.2020	08.03.2020
31.08.2020	03.09.2020	09.03.2020	14.03.2020
05.09.2020	11.09.2020	28.03.2020	10.04.2020
03.11.2020	07.11.2020	19.04.2020	27.05.2020
21.11.2020	25.11.2020	9.11.2020	15.11.2020
23.02.2021	27.02.2021	12.12.2020	22.12.2020
09.03.2021	12.03.2021	30.12.2020	06.01.2021
		21.01.2021	20.02.2021
		28.02.2021	07.03.2021
		13.03.2021	24.03.2021
		29.03.2021	07.04.2021

137 **Table 1** Streamer events above Northern Atlantic from January 2020 until March 2021 and  
138 related start and end dates. The right part shows calm periods.



139

140 Figure 1 shows the TO3 by TOPOMI/S5P integrated from November 3<sup>rd</sup> to November 5<sup>th</sup>  
141 2020. Ozone-poor airmasses (blue) are located above the Northern Atlantic from 30°N to  
142 70°N next to smaller scale ozone-poor airmasses above western North America and Central  
143 Asia. The TO3 concentration is disturbed by planetary waves along the latitudes, which lead  
144 to wave structures visible especially at the transition of blue to green colors. A large streamer  
145 event of ozone-poor airmasses is detected over the Northern Atlantic. A small streamer can be  
146 detected over western North America. There are also ozone-poor air masses above eastern  
147 Europe. The temporal evolution shows, that the ozone-poor air masses above eastern Europe  
148 are due to a decaying streamer which evolved several days earlier. As planetary waves are  
149 more or less permanently disturbing the atmospheric dynamics, especially smaller scale  
150 streamers can be detected almost every day. In this example, the streamer event above the  
151 Northern Atlantic is largest. Therefore, we consider this event for the further analysis.



152

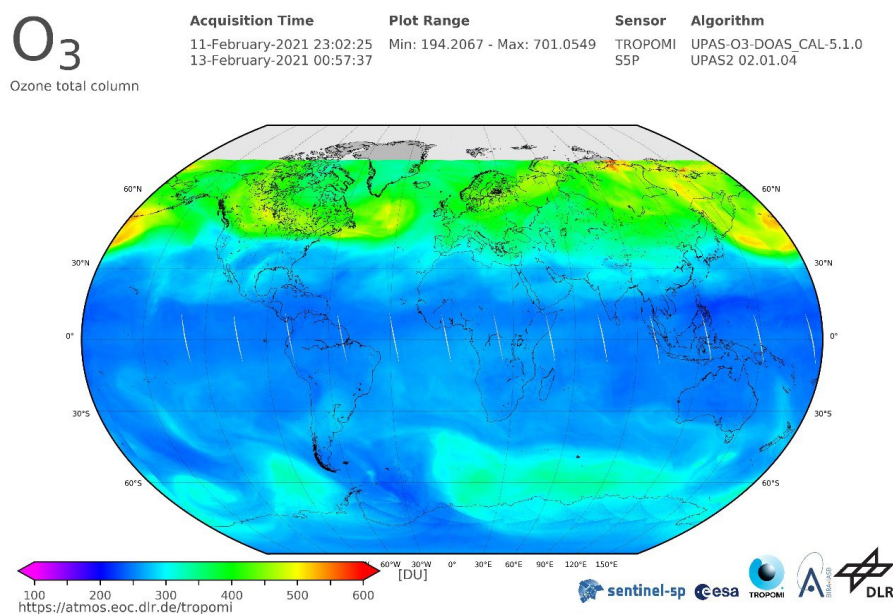
153 Fig. 1. TO3 by TROPOMI/S5P from November 3<sup>rd</sup> to November 5<sup>th</sup> 2020 shows ozone poor  
154 airmasses above the Northern Atlantic as an example of a streamer event for the further  
155 analysis. Colors (from violet to red) indicate the total ozone column concentrations (from low  
156 to high) in Dobson Units. Source: DLR, CC-BY 3.0

157



158 Figure 2 shows the TO3 by TOPOMI/S5P from February 11<sup>th</sup> to February 13<sup>th</sup> 2020. The  
159 event is characterized by a strong meridional gradient from the equatorial to polar region on  
160 the Northern Hemisphere with almost no longitudinal variation. Therefore, we consider this  
161 event for the further analysis.

162



164 Fig. 2. TO3 by TROPOMI/S5P from February 11<sup>th</sup> to February 13<sup>th</sup> 2020 as an example of  
165 calm atmospheric dynamics. A clear meridional gradient of ozone can be observed on the  
166 Northern Hemisphere without large-scale wave structures. Colors (from violet to red) indicate  
167 the total ozone column concentrations (from low to high) in Dobson Units. Source: DLR, CC-  
168 BY 3.0

169 Two stations of the Czech microbarograph network, (Bondar et al., 2022) are involved in the  
170 study – the large aperture array WBCI (50.25°N 12.44°E) and the small aperture array PVCII  
171 (50.52°N 14.57°E). To study propagation of GW and long-period infrasound (from acoustic  
172 cut-off up to about 2.5 s) pressure recordings at WBCI are utilized. Four sensors of the WBCI  
173 array are arranged in a tetragon The inter-element distances of 4 – 10 km define an optimum  
174 performance of the array in the infrasound frequency range from the acoustic cut-off  
175 frequency of 0.0033 to 0.0068 Hz (Garcès, 2013). The WBCI array with its large inter-  
176 element distances has a unique configuration compared to the arrays of the International  
177 Monitoring System of the Comprehensive Nuclear Test Ban Treaty Organisation intended  
178 for infrasound monitoring in the frequency band of 0.02 – 4 Hz (Marty, 2019). Each array



179 element at WBCI is equipped with an absolute microbarometer of the type Paroscientific  
180 6000-16B-IS with parts-per-billion resolution. Sampling frequency is 50 Hz and a GPS  
181 receiver is used for time stamping. In infrasound studies, data resampled at 10 Hz sampling  
182 rate are used. To detect and analyze GW, 1-min mean values are used.

183 The small aperture array PVEC provides optimal precision of detections in the frequency  
184 range of 0.14 – 3.4 Hz (Garcès, 2013). Three sensors are arranged in an equilateral triangle;  
185 the array aperture is 200 m. The differential sensors of the type Infrasound Gage ISGM03  
186 manufactured by the Scientific and Technical Centre give a flat response in the frequency  
187 range of 0.02 – 4 Hz. The data are stored with a sampling frequency of 25 Hz; a GPS receiver  
188 is used for time stamping.

189 Infrasound detections at WBCI and at PVEC are processed using the Progressive Multi-  
190 Channel Correlation (PMCC) detection algorithm (Cansi, 1995; Le Pichon and Cansi, 2003).  
191 The PMCC configuration is set on an individual basis and is optimized for the given array  
192 (Brachet et al., 2010; Garcès, 2013; Szuberla et al., 2004). From the resulting PMCC  
193 detection bulletins infrasound arrival parameters of interest are extracted and used in the  
194 statistical analysis: time of arrival, root-mean-square (RMS) amplitude, azimuth of arrival,  
195 and mean frequency.

196 Propagation of GW in the thermosphere/ionosphere is studied using multi-point and multi-  
197 frequency continuous Doppler sounding system located in Czechia. Its advantage is a high  
198 time resolution (around 10 s) compared with ionospheric sounders (ionosondes) that measure  
199 the profile of electron densities in the ionosphere. The continuous Doppler sounding is based  
200 on the measurement of Doppler frequency shift experienced by radio waves that reflect from  
201 the ionosphere. The propagation characteristics of GWs are calculated from the time delays  
202 between signals observed at the respective sounding paths (transmitter-receiver pairs). The  
203 methods are in detail described by Chum and Podolska (2018). The two-dimensional (2-D)  
204 version (propagation analysis in horizontal plane only) is anticipated for most of the studies,  
205 since a 3-D analysis requires simultaneous observation and signal correlation at different  
206 frequencies, which is often not the case, especially during solar minimum. Results of  
207 statistical investigation have been recently published (Chum et al., 2021). Identical methods  
208 of propagation analysis have been applied to investigate propagation of GWs in the  
209 troposphere based on data from large-aperture array WBCI.





210 All analysis will be done with respect to streamer events the occurrence of which is shown in  
211 Table 1. We analyze winter period from 6 February 2020 to 7 April 2021. Calm periods can  
212 be found also in Table 1.

213

### 214 **3) Results**

#### 215 **3.1 Infrasound observations at ground stations WBCI and PVICI during streamer** 216 **events 2020 – 2021**

217 As in detail explained in the introduction, we investigate whether ground infrasound  
218 measurements can serve as a quick indicator of streamer events. Therefore, we compare  
219 infrasound detections during streamers with observations on calm days. Distinct differences  
220 are searched for, that can be revealed in routine processing of data from a microbarograph  
221 array. At first, we make a visual comparison of 2-D histograms of infrasound arrival  
222 parameters. Then mean values of two data sets – streamer events and calm days – are  
223 compared; a two-choice hypothesis test using the central limit theorem is applied at the  
224 significance level  $\alpha = 0.05$ .

$$225 \quad u = \frac{\bar{x} - \bar{y}}{\sqrt{\frac{s_x^2}{n_x} + \frac{s_y^2}{n_y}}}$$

226 Where  $u$  is the test criterion,  $\bar{x}$  and  $\bar{y}$  are the means of the first and second data set,  $s_x^2$  and  $s_y^2$   
227 are the variances, and  $n_x$  and  $n_y$  are the numbers of elements in the first and second data set,  
228 respectively. A normal distribution of  $u$  is expected when the mean values are equal.

##### 229 **3.1.1 Observations at WBCI during streamer events 2020 – 2021**

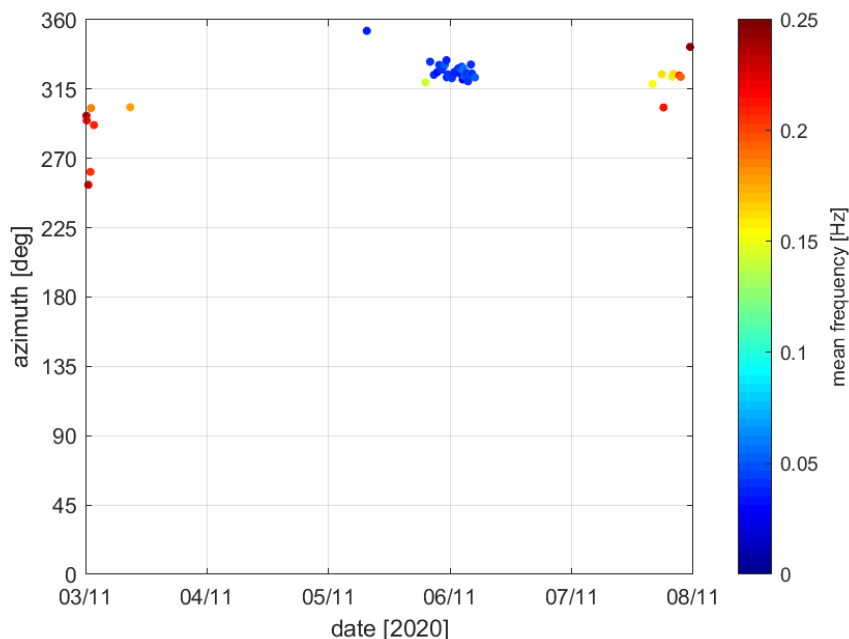
230 Wave activity in the infrasound frequency range of 0.0033 – 0.4 Hz was investigated. The  
231 upper limit of the analysed band was set so that it includes microbaroms, although the  
232 operational range of the array was thus extended towards higher frequencies compared with  
233 the optimum array range (0.0033 – 0.0068 Hz) (Garcès, 2013).

234 Microbaroms are generated by a non-linear interaction of ocean waves travelling in opposite  
235 directions. Microbarom frequency corresponds to twice the frequency of sea waves.  
236 Microbaroms form a wide spectral peak around 0.2 Hz. A powerful source of microbaroms is  
237 located in the North Atlantic and the signals are regularly detected by European infrasound



238 stations (Hupe et al., 2018). The detection capability of microbaroms from the North Atlantic  
239 is high particularly from October to March when the source becomes stronger due to stormy  
240 weather above the ocean and signal propagation to the East from the source is supported by  
241 the stratospheric waveguide (Landès et al., 2012). From the global point of view,  
242 microbaroms are permanently present in recordings of infrasound stations worldwide.

243 A strong streamer event occurred on 3<sup>rd</sup> – 7<sup>th</sup> November 2020. WBCI recorded infrasound in  
244 a few sparse intervals on 3<sup>rd</sup> November at 00-09 UTC, on 5<sup>th</sup> – 6<sup>th</sup> November at 19-05 UTC,  
245 and on 7<sup>th</sup> November at 16-24 UTC from back-azimuths of 250° – 305° and later from back-  
246 azimuths of 305° – 340° (Figure 3). The signal frequencies on 5<sup>th</sup> – 6<sup>th</sup> November differed  
247 from those on 3<sup>rd</sup> November and 7<sup>th</sup> November: frequencies of ~0.04 Hz were observed on 5<sup>th</sup>  
248 – 6<sup>th</sup> November while on 3<sup>rd</sup> and 7<sup>th</sup> November they were around 0.2 Hz.



249

250 **Figure 3** Infrasound observations at WBCI on 3<sup>rd</sup> – 7<sup>th</sup> November 2020. Azimuth of signal  
251 arrival is shown; the colorbar refers to the mean frequency of the detection family. A detection  
252 family is a group of primary PMCC detections-so called detection pixels- merged together  
253 based on similarity of arrival parameters carried by the pixels. One circle in the plot  
254 represents one detection family.

255



256     Infrasound detections were sparse also in the other studied streamer events and calm  
257     periods. The streamer events occurred on 35 days between February 2020 and April 2021,  
258     247 infrasound detections were obtained. Within the same time window, 867 infrasound  
259     detections on 153 calm days were found. To avoid possible distortion of the results due to a  
260     single extreme value in a small dataset, we did not evaluate the infrasound arrival parameters  
261     during the respective streamers, but we grouped the observation in an overall data set and  
262     compared its mean values against the reference group of all calm days within the studied time  
263     period. We cannot reject that signal amplitudes are same during streamer events and on calm  
264     days at the significance level  $\alpha = 0.05$ . Mean signal frequency is higher in the group of days  
265     with streamer events at the significance level  $\alpha = 0.05$ , or with 95% reliability. Details are  
266     presented in Table 2. and visually can be seen on Figure 4. Notice that contrary to the result  
267     for the overall data sets, the signal frequencies transiently decreased from  $\sim 0.2$  Hz to  $\sim 0.04$   
268     Hz during the strong streamer on 3<sup>rd</sup> – 7<sup>th</sup> November 2020. Besides possible influences of  
269     changed dynamics in the lower/middle atmosphere on infrasound propagation, modification  
270     of the infrasound source shall be considered on 3<sup>rd</sup> – 7<sup>th</sup> November 2020. There was a large  
271     pressure gradient above the North Atlantic (earth.nulschool.net, www2.wetter3.de,  
272     [www.ventusky.com](http://www.ventusky.com)). The WAVEWATCHIII<sup>®</sup> wave-action model (The WAVEWATCHIII<sup>®</sup>  
273     Development Group, 2016) predicted an increase of significant height of combined wind  
274     waves and swell in the North Atlantic particularly on 5<sup>th</sup> – 6<sup>th</sup> November 2020; the peak wave  
275     periods stayed in the interval from 10 to 15 s on 3<sup>rd</sup> – 7<sup>th</sup> November 2020 (plots not shown  
276     here). To investigate properly the influence of source-related and signal-propagation factors  
277     on infrasound detections at WBCI during the streamer event, a complex study including  
278     infrasound source and propagation modeling is necessary. However, this is out of the scope of  
279     the present paper and it can be performed in a future dedicated study.

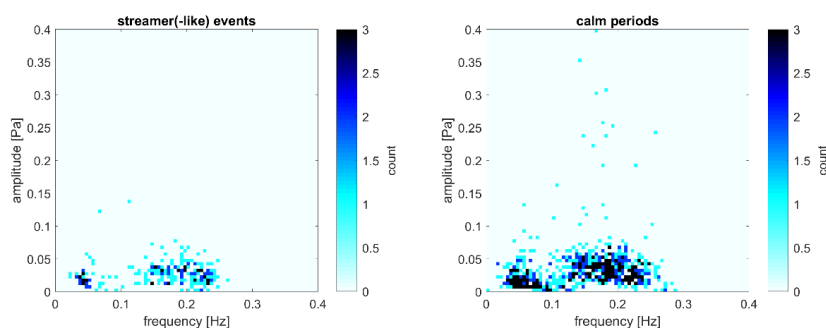
280

	mean	variance	number of detections
Frequency [Hz], calm days	0.147	0.005	867
Frequency [Hz], streamer events	0.160	0.005	247
RMS amplitude [Pa], calm days	0.043	0.019	867



RMS amplitude [Pa], streamer events	0.039	0.012	247
----------------------------------------	-------	-------	-----

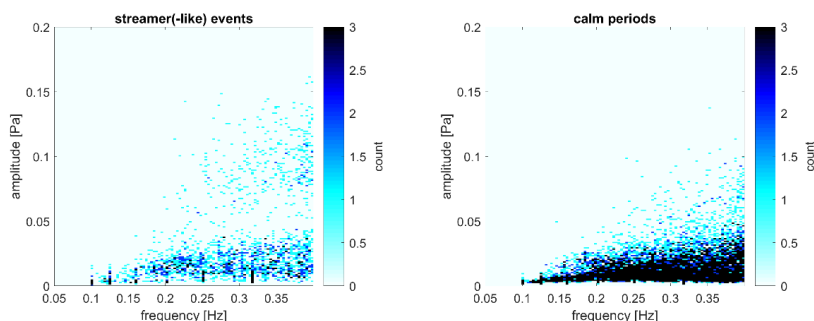
281 **Table 2** Mean and variance of infrasound arrival parameters at WBCI during streamer  
282 events and on calm days and number of detections.  
283



284

285 **Figure 4** 2D histogram frequency vs. amplitude of signals measured at WBCI. Left panel:  
286 summary of streamer events 2020 – 2021, right panel: calm period 2020 – 2021 as reference  
287 data. The colorbar shows number of detections in the respective frequency-amplitude bins.

288



289

290 **Figure 5** 2D histogram frequency vs. amplitude of signals measured at PPCI. Left panel:  
291 summary of streamer events (3<sup>rd</sup> – 7<sup>th</sup> November 2020, 21<sup>st</sup> – 25<sup>th</sup> November 2020, and 9<sup>th</sup> –  
292 12<sup>th</sup> March 2021), right panel: calm periods as reference data (2<sup>nd</sup> – 14<sup>th</sup> March 2020, 9<sup>th</sup> –  
293 15<sup>th</sup> November 2020, 18<sup>th</sup> – 22<sup>nd</sup> December 2020, 1<sup>st</sup> – 7<sup>th</sup> March 2021, and 14<sup>th</sup> – 24<sup>th</sup>  
294 March 2021). The color bar shows number of detections in the respective frequency-  
295 amplitude bins

296

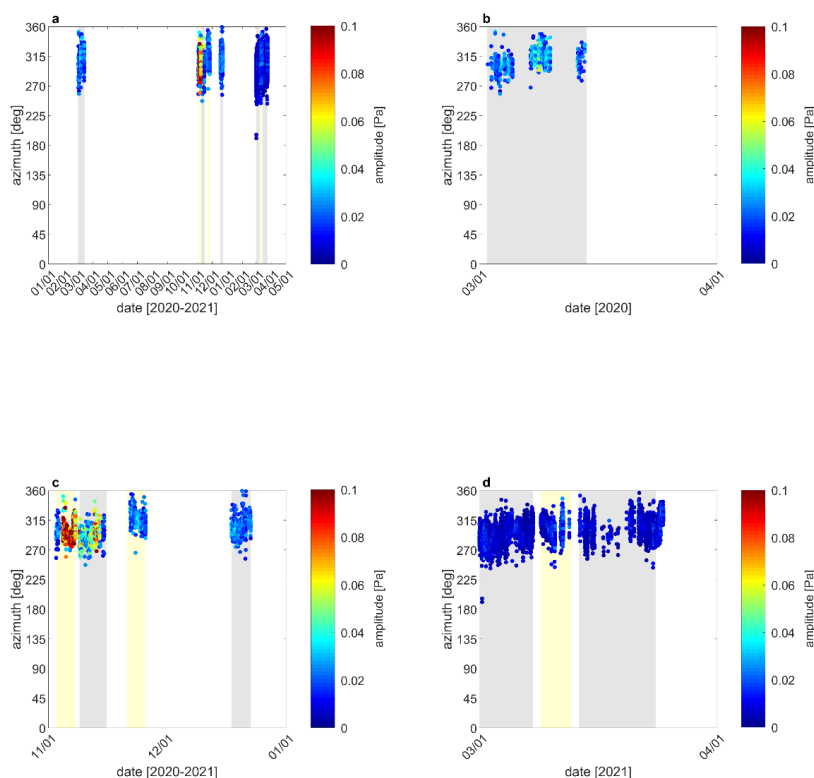
### 297 3.1.2 Observations at PPCI

298 The performance of the WBCI array at the upper limit of the frequency band of interest, the  
299 microbarom band can be degraded. Therefore, the PPCI array is included in the study the  
300 performance of which is optimal in the 0.12 – 0.35 Hz microbarom band.

301 Infrasound detections for selected streamer events were analysed: 3<sup>rd</sup> – 7<sup>th</sup> November 2020,  
302 21<sup>st</sup> – 25<sup>th</sup> November 2020, and 9<sup>th</sup> – 12<sup>th</sup> March 2021 (Figures 5 and 6). PPCI data were not  
303 available for most of the streamer event periods on 6<sup>th</sup> – 10<sup>th</sup> February 2020 and on 23<sup>rd</sup> – 27<sup>th</sup>  
304 February 2021. We focused on streamer events that occurred in the season of winter  
305 stratospheric westerlies, which lasts usually from November to March (Le Pichon et al. 2012).  
306 In winter, infrasound stations largely detect sources located to the west from the station.



307 Streamer events typically occur above Western Europe and adjacent regions of the North  
308 Atlantic. Therefore, winter is the season, when Central European infrasound stations are able  
309 to detect signals arriving from or through the regions of streamer events. Observations during  
310 calm periods on 2<sup>nd</sup> – 14<sup>th</sup> March 2020, 9<sup>th</sup> – 15<sup>th</sup> November 2020, 18<sup>th</sup> – 22<sup>nd</sup> December  
311 2020, 1<sup>st</sup> – 7<sup>th</sup> March 2021, and 14<sup>th</sup> – 24<sup>th</sup> March 2021 were used as a reference data set.



312

313 **Figure 6** Infrasound detections at PVCi during streamer events (yellow fields) and calm  
314 periods (grey fields) in 2020 and 2021. Azimuth of signal arrival is shown; the color bar refers  
315 to the signal amplitude. Panel (a): overview plot of all analyzed periods; panels (b) – (d):  
316 zoom at March 2020, November – December 2020, and March 2021



317 Taking into account the mutual positions of PPCI and the region of typical occurrence of  
318 streamers, we analysed signals arriving from the back-azimuths of 180 – 360°. We focused on  
319 detections in the frequency range of 0.05 – 0.4 Hz. The band partly overlaps with the  
320 detection range of the WBCI array (0.0033 – 0.4 Hz) and at frequencies of 0.12 – 0.35 Hz it is  
321 dominated by microbaroms (e.g., Campus and Christie, 2010).  
322 High sensitivity of the PPCI array in the microbarom frequency range enabled to compare the  
323 respective streamer events with the reference data separately. As we focus on signal analysis  
324 in a narrow frequency range (0.05 – 0.4 Hz), signal frequency during streamer events and its  
325 departures from calm-day values were not analyzed. Higher mean signal amplitude was  
326 proved on the significance level  $\alpha = 0.05$ , or with 95% reliability during the streamer events  
327 on 3<sup>rd</sup> – 7<sup>th</sup> November 2020 and 21<sup>st</sup> – 25<sup>th</sup> November 2020. It was not rejected that the signal  
328 amplitudes during streamer event on 9<sup>th</sup> – 12<sup>th</sup> March 2021 are same as on the calm days.  
329 Details can be found in Table 3. The highest difference of signal amplitudes compared to the  
330 set of calm days was found during the streamer on 3<sup>rd</sup> – 7<sup>th</sup> November 2020; mean signal  
331 amplitude of 0.013 Pa was obtained on the calm days, whereas on 3<sup>rd</sup> – 7<sup>th</sup> November the  
332 mean amplitude increased to 0.077 Pa. As discussed in section 3.2.1, the microbarom source  
333 in the North Atlantic was possibly intensified by a maritime storm that was in progress during  
334 the considered time interval.  
335

	mean	variance	number of detections
RMS amplitude [Pa], calm days	0.013	< 0.001	11343
RMS amplitude [Pa], streamer event 3-7 November 2020	0.077	0.001	482
RMS amplitude [Pa], streamer event 21-25 November 2020	0.024	< 0.001	360
RMS amplitude [Pa], streamer event 9-12 March 2021	0.013	< 0.001	1543

336 **Table 3** Mean and variance of the RMS amplitude and number of detections at PPCI in the  
337 set of calm days and during the respective streamer events.



338

### 339 **3.2 Results and discussion of gravity waves in the troposphere and ionosphere**

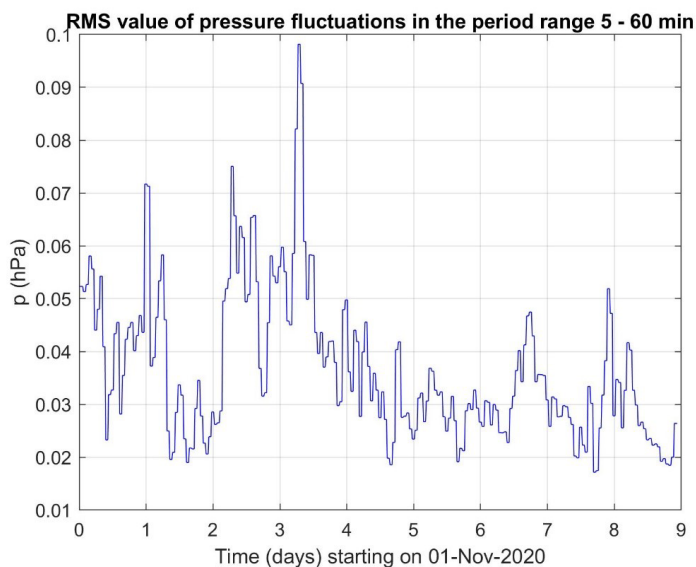
340

#### 341 **3.2.1 Investigation of GWs measured on the ground by WBCI array of micro-** 342 **barometers.**

343 . Figure 7 shows the RMS amplitudes of pressure fluctuations in the period range 5-60 min  
344 recorded from November 1 to November 9, 2020. This interval covers a distinct streamer  
345 event that occurred from November 3 to November 7. The results of propagation analysis are  
346 shown in Figure 8, which displays the phase velocities and azimuths of GWs. Only results  
347 that satisfied the criterion ( $dv/v < 0.0.5$ ) and ( $dAZ < 10^\circ$ ) and ( $p_{RMS} > 0.02$  Pa) are presented,  
348 where  $dv/v$ ,  $dAZ$ ,  $p_{RMS}$  are the relative uncertainty of GW phase velocity, uncertainty of  
349 azimuth and root mean square value of pressure fluctuations in the analysed time interval.  
350 Figure 8 demonstrates that there is a tendency for higher phase velocities and occurrence of  
351 different azimuths during the streamer event. Therefore, it is useful to compare the GW  
352 characteristics during streamer events and calm conditions.

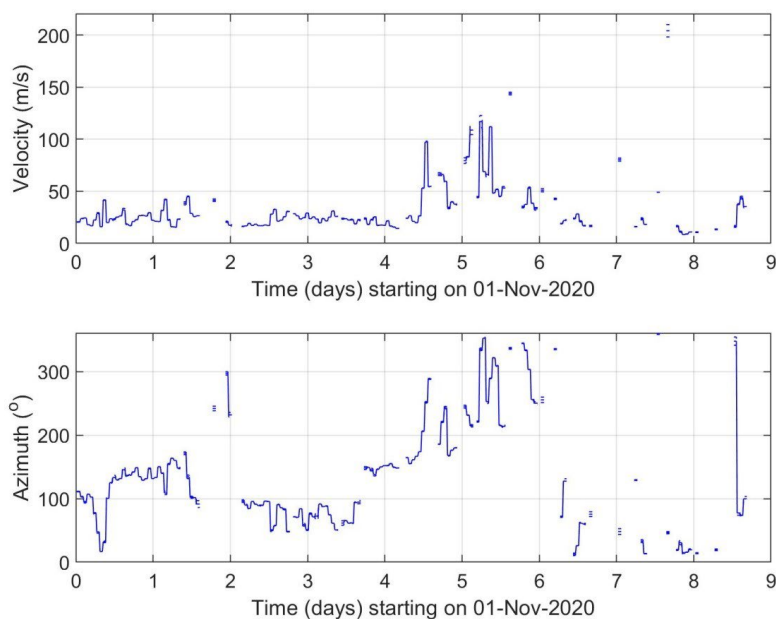
353 Figure 9 shows histograms obtained by a statistical analysis. The RMS amplitudes of  
354 pressure fluctuations in the period range 5 – 60 min, phase velocities and azimuths were  
355 investigated separately for calm conditions (upper plots) and for streamer and streamer-like  
356 events listed in Table 1 (bottom plots). The solid vertical lines mark lower (Q1) and upper  
357 (Q3) quartiles. The dashed vertical lines depict boundaries for large ( $Q3 + 1.5 \cdot (Q3 - Q1)$ ) and  
358 extreme ( $Q3 + 3 \cdot (Q3 - Q1)$ ) values. A difference between histograms for RMS pressure  
359 fluctuations and azimuths obtained for calm and disturbed conditions is obvious. A minor  
360 difference is also observed for phase velocities.





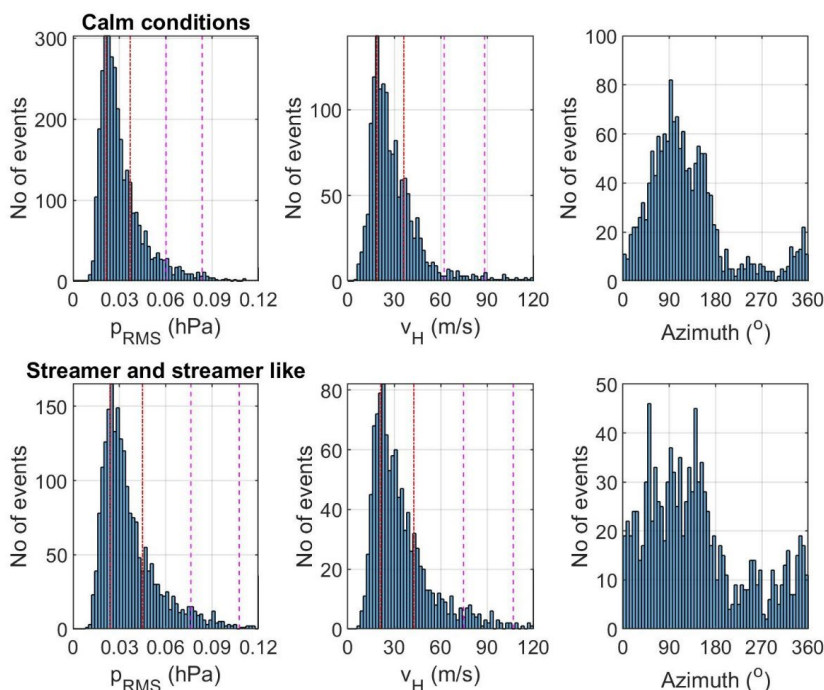
361

362 **Figure 7** Amplitude of GWs recorded by WBCI from 2020-11-01 to 2020-11-09



363

364 **Figure 8** Propagation velocity and azimuth of GWs recorded by WBCI from 2020-11-01 to  
365 2020-11-09



366

367 **Figure 9** GW characteristics (RMS of pressure fluctuations, phase velocity and azimuth) for  
368 calm periods (upper plots) and streamer and streamer like events (bottom plots) for 2020 and  
369 winter 2021. The red vertical lines mark lower (Q1) and upper (Q3) quartiles. The dashed  
370 magenta vertical lines depict boundaries for large ( $Q3+1.5\cdot(Q3-Q1)$ ) and extreme ( $Q3+3\cdot(Q3-$   
371  $Q1)$ ) values.

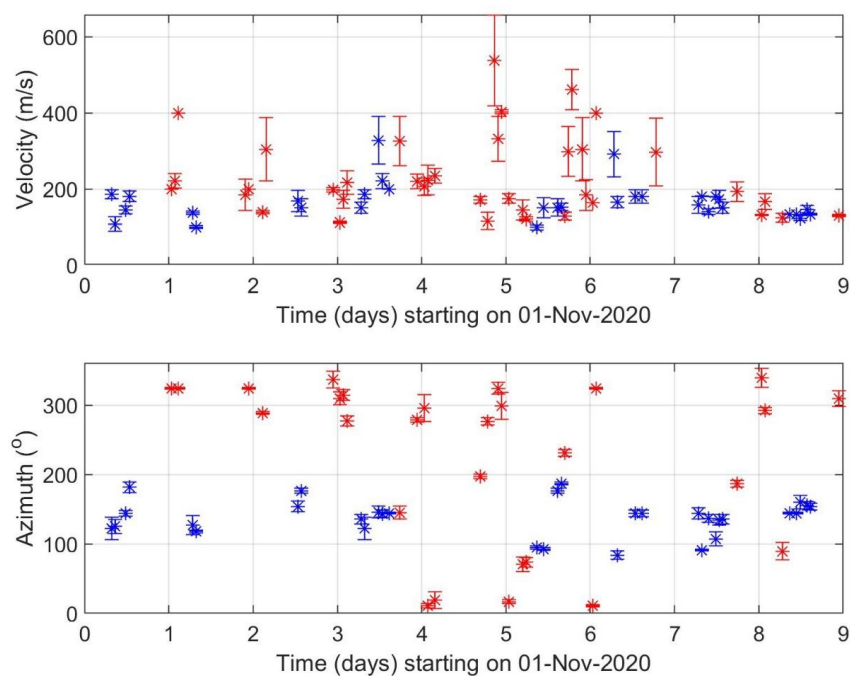
372

### 373 3.2.2 Investigation of GWs measured in the ionosphere by continuous Doppler 374 sounding system (CDS)

375 The 2D propagation analysis of GWs was performed using the 2D versions of methods  
376 mentioned in Section 2 and in detail described by Chum and Podolská (2018). The 2D  
377 propagation analysis makes it possible to analyze much larger number of time intervals than  
378 the 3D analysis (Chum et al., 2021). The propagation analysis obtained for the interval from  
379 1<sup>st</sup> November to 9<sup>th</sup> November 2020, which covers the significant streamer event that occurred  
380 from 3<sup>rd</sup> November 2020 to 7<sup>th</sup> November 2020, is presented in Figure 10. Only results that  
381 satisfied the criterion ( $dv/v < 0.2$ ) and ( $dAZ < 20^\circ$ ) and ( $f_{DRMS} > 0.05$  Hz) and ( $C_{max} < 0.5$ ) are



382 presented, where  $dv/v$  is the relative uncertainty of GW phase velocity,  $dAZ$  is the azimuth  
383 uncertainty,  $f_{DRMS}$  is the root mean square of the Doppler shift in the analysed time interval  
384 and  $C_{max}$  is the maximum in the normalized energy map for the best beam (slowness) search;  
385  $C_{max}$  is 1 for identical signals (Chum and Podolská, 2018). It is considered that signals are not  
386 sufficiently correlated (coherent) for reliable propagation analysis if  $C_{max} < 0.5$  (Chum et al.,  
387 2021). The velocities and azimuth obtained by observation at 3.59 MHz are in red, whereas  
388 the values based on measurements at 4.65 MHz are in blue. Obviously, the observations at  
389 3.59 MHz mostly corresponds to the nighttime, whereas observations at 4.65 MHz were  
390 mostly made during the daytime. The GWs usually propagated roughly poleward at night and  
391 roughly equatorward during the daytime. This is fully consistent with the statistical  
392 investigation (Chum et al., 2021) who showed that propagation directions of GWs in the  
393 ionosphere exhibit diurnal and seasonal behaviour and are mainly controlled by the neutral  
394 winds in the thermosphere.



395

396 **Figure 10** Propagation velocity and azimuth of GWs in the ionosphere obtained using CDS  
397 measurements from 2020-11-01 to 2020-11-09. The velocities and azimuth obtained by



398 observation at 3.59 MHz are by red, whereas the values based on measurements at 4.65 MHz  
399 are by blue.

400 Based on the analysis of the GW observed in the ionosphere during the streamer event and  
401 on the previous statistical analysis, we conclude that no obvious signature related to streamer  
402 event was observed for the propagation of GW the ionosphere.

403 It should be also mentioned that the phase velocities of GW measured on the ground (Figure  
404 8) and at heights around 200 km in the ionosphere differ. There are several reasons for that.  
405 First, the observed horizontal phase velocities depend on the elevation angle of GW  
406 propagation and on the ambient temperature as follows from the dispersion relation (the  
407 temperature enters the dispersion relation via the buoyancy frequency and the scale height).  
408 The temperature in the ionosphere/thermosphere is several times higher than in the  
409 troposphere. The elevation angles might change during the upward propagation of GWs,  
410 depending on the wind and temperature profile. Second, GWs propagate with a tilt, not  
411 vertically upward. It is therefore highly probable that the sources of the GWs observed in the  
412 troposphere and ionosphere are different. Moreover, GW can break during their propagation  
413 upward and secondary gravity waves might be observed in the ionosphere.

#### 414 **4) Conclusion and discussion**

415 The focus of this study was to test independent types of observations like Doppler sounding  
416 and microbarograph measurements for an analysis of GW behavior during streamer events,  
417 which are strongly connected with PW or GW and the large scale mass transport of ozone and  
418 that is why it can be very interesting for studies of atmospheric dynamics.

419 The other aim of the study was to find phenomena in infrasound arrival parameters that  
420 could serve as a quick indicator of streamers and that could be identified in routine processing  
421 of infrasound detections. Simple visual comparison of infrasound arrivals during streamer  
422 events and on calm days (Figures 4 – 6) did not reveal significant and easy-to-identify  
423 deviations of the arrival parameters – the azimuth of arrival, RMS signal amplitude and signal  
424 frequency. The statistical analysis showed larger signal amplitudes at PPCI during two of  
425 three analysed streamers (Table 3). At WBCI, it was not rejected that signal amplitudes are  
426 same during streamer events and on calm days (Table 2). Higher signal frequencies were  
427 proved at WBCI in the streamer events data set than in the calm days data set. Yet, during the  
428 strong streamer event on 3<sup>rd</sup> – 7<sup>th</sup> November 2020, a transient decrease of the frequency of



429 detected signal was recorded at WBCI. Based on these results, infrasound measurement at a  
430 single infrasound station cannot be recommended as a reliable sole indicator of streamers.

431 Streamer events are limited in time and space. The observations of signatures of a streamer  
432 at an infrasound array can depend on the mutual positions of the source, the streamer region,  
433 and the observer. It is therefore suggested to analyse infrasound arrival parameters at a dense  
434 network of infrasound arrays that covers various directions and distances from the streamer  
435 region in order to reveal possible streamer event indicators. To explain properly the influence  
436 of streamers on infrasound propagation a dedicated 3D model study of infrasound propagation  
437 can be recommended. Infrasound sources in the present study were not well defined in terms  
438 of location, time, and intensity. Taking into account the aim of the present study –  
439 identification of an easy accessible and quick indicator of streamers in infrasound  
440 measurements, our results show some limitation but on the other hand it will be to benefit of  
441 future studies, if sources of the analyzed signals are better known and more events will be  
442 used for statistics.

443 Supplementary ground-based measurements of GW using the WBCI array in the  
444 troposphere showed that GW propagation azimuths were more random during streamer and  
445 streamer-like events compared to those observed during calm conditions. At the same time,  
446 larger GW amplitudes were observed in the troposphere during streamer and streamer-like  
447 events than under quiescent conditions. On the other hand, the GW propagation  
448 characteristics observed in the ionosphere by CDS during streamer events did not differ from  
449 those expected for the given time period, based on previous statistical studies (Chum et al.,  
450 2021).

451 More streamer events would need to be analysed to verify these preliminary results based on  
452 the limited number of events.

453 **Data availability:** WAVEWATCHIII data at

454 <https://polar.ncep.noaa.gov/waves/ensemble/download.shtml>, accessed on 14 March 2023

455 ozone column measurements (TO3) which are available as a service by DLR at

456 <https://atmos.eoc.dlr.de/>

457 **Author contributions**

458 MK and LK create the idea of manuscript; JCh, MK, TS, LK, and KP suggest the datasets and  
459 methods; TS, JCh, LK, KP and FT analyzed the data; MK wrote the manuscript draft; JCh,  
460 TS, LK and KP reviewed and edited the manuscript.



461 **Competing interests**

462 The authors declare that they have no conflict of interest.

463

464 **Acknowledgement**

465 The DTK-GPMCC software was kindly provided by Commissariat à l'énergie atomique et  
466 aux énergies alternatives, Centre DAM-Île-de-France, Département Analyse, Surveillance,  
467 Environnement, Bruyères-le-Châtel, F91297 Arpajon, France.

468 **Financial support:** This study is supported by LISA project- Lidar measurements to  
469 Identify Streamers and analyze Atmospheric waves, AEOLUS-INNOVATION, Contract No.  
470 4000133567/20/I-BG

471

472 **References**

473 Assink, J.D., Waxler, R., Smets, P., Evers, L.G. (2014). Bidirectional infrasonic ducts  
474 associated with sudden stratospheric warm-ing events. *J. Geophys. Res. Atmos.* 119,1140-  
475 1153.

476 Blixt, E.M., Nasholm, S.P., Gibbons, S.J., Evers, L.G., Charlton-Perez, A.J., Orsolini, Y.J.,  
477 Kvaerna, T. (2019). Estimating tropo-spheric and stratospheric winds using infrasound from  
478 explosions. *J. Acoust. Soc. Am.* 146:2.

479 Brachet, N., Brown, D., Le Bras R., Cansi, Y., Mialle, P., Coyne, J. (2010). Monitoring the  
480 Earth's Atmosphere with the Global IMS Infrasound Network. In: Le Pichon, A., Blanc, E.,  
481 Hauchecorne A. (Eds.), *Infrasound Monitoring for Atmospheric Studies*. Springer  
482 Science+Business Media B.V., 77-118. Doi: 10.1007/978-1-4020-9508-5\_3

483 Bondár I., T. Šindelářová, D. Ghica, U. Mitterbauer, A.Liashchuk, J. Baše, J. Chum, C.  
484 Czanik, C. Ionescu, C. Neagoe, M. Pásztor, A. Le Pichon (2022), Central and Eastern  
485 European Infrasound Network: Contribution to Infrasound Monitoring, *Geophys. J. Int.*,  
486 ggac066, <https://doi.org/10.1093/gji/ggac066>

487 Campus, P., Christie, D.R. (2010). Worldwide Observations of Infrasonic Waves. In: Le  
488 Pichon, A., Blanc, E., Hauchecorne A. (Eds.), *Infrasound Monitoring for Atmospheric*



- 489 Studies. Springer Science+Business Media B.V., 185234-118. Doi: 10.1007/978-1-4020-  
490 9508-5\_6
- 491 Cansi, Y., 1995. An automatic seismic event processing for detection and location: The  
492 P.M.C.C. method. *Geophys. Res. Lett.* 22, 1021-1024. doi: 10.1029/95GL00468
- 493 Ceranna, L., Matoza, R., Hupe, P., Le Pichon, A., Landès, M., (2019). Systematic Array  
494 Processing of a Decade of Global IMS Infrasound Data. In: Le Pichon, A., Blanc, E.,  
495 Hauchecorne, A. (eds) *Infrasound Monitoring for Atmospheric Studies. Challenges in*  
496 *Middle Atmospheric Dynamics and Societal Benefits*. Springer Nature Switzerland AG.
- 497 Chum J, Podolská K (2018) 3D analysis of GW propagation in the ionosphere. *Geophysical*  
498 *Research Letters*, 45, 11,562–11,571, <https://doi.org/10.1029/2018GL07969>
- 499 Chum, J., Podolská, K., Ruzs, J., Baše, J., Tedoradze, N. (2021), Statistical investigation of  
500 gravity wave characteristics in the ionosphere. *Earth Planets Space* 73, 60,  
501 <https://doi.org/10.1186/s40623-021-01379-3>
- 502 Evers, L. G., Siegmund, P. (2009). Infrasonic signature of the 2009 major sudden  
503 stratosphericwarming, *Geophys. Res. Lett.*, 36, L23808, doi:10.1029/2009GL041323
- 504 Evers, L.G., Haak, H.W. (2010). The Characteristics of Infrasound, its Propagation and Some  
505 Early History. In: Le Pichon, A., Blanc, E., Hauchecorne, A. (eds) *Infrasound Monitoring for*  
506 *Atmospheric Studies*. Springer, Dordrecht.
- 507 Evers, L. G., van Geyt, A. R. J. , Smets, P., Fricke, J.T. (2012). Anomalous infrasound  
508 propagation in a hot stratosphere and the existence of extremely small shadow zones, *J.*  
509 *Geophys. Res.*, 117, D06120, doi:10.1029/2011JD017014.
- 510
- 511 Eyring, V., Dameris, M., Grewe, V., Langbein, I., & Kouker, W. (2002). Climatologies of  
512 streamer events derived from a transport model and a coupled chemistry-climate model.
- 513 Fritts, D.C. & Alexander, M.J., (2003). Gravity wave dynamics and effects in the middle  
514 atmosphere. *Rev. Geophys.*, 41 (1), 1003.



- 515 Garcès, M., Willis, M., Hetzer, C., Le Pichon, A., Drob, D., (2004). On using ocean swells  
516 for continuous infrasonic measurements of winds and temperature in the lower, middle, and  
517 upper atmosphere. *Geophys. Res. Lett.* 31, L19304. doi: 10.1029/2004GL020696
- 518 Garcès, M.A., (2013). On infrasound standards, part 1: Time, frequency, and energy scaling.  
519 *InfraMatics* 2, 13-35. doi: 10.4236/inframatics.2013.22002
- 520 Gerlach, C., Földvary, L., Švehla, D., Gruber, T., Wermuth, M., Sneeuw, N., ... &  
521 Steigenberger, P. (2003). A CHAMP-only gravity field model from kinematic orbits using the  
522 energy integral. *Geophysical Research Letters*, 30(20).
- 523 Hersbach, H., Bell, B., Berrisford, P., Hirahara, S., Horányi, A., Muñoz-Sabater, J., ... &  
524 Thépaut, J. N. (2020). The ERA5 global reanalysis. *Quarterly Journal of the Royal*  
525 *Meteorological Society*, 146(730), 1999-2049.
- 526 Hupe, Patrick, Lars Ceranna, and Christoph Pilger. (2018). "Using barometric time series of  
527 the IMS infrasound network for a global analysis of thermally induced atmospheric  
528 tides." *Atmospheric Measurement Techniques* 11.4 2027-2040.
- 529 James, P. M. (1998): A climatology of ozone mini-holes over the Northern Hemisphere.  
530 *International Journal of Climatology: A Journal of the Royal Meteorological Society*, 18, 12:  
531 12871303
- 532 Kramer, R, S. Wüst, and M. Bittner (2016). Investigation of gravity wave activity based on  
533 operational radiosonde data from 13 years (1997-2009): Climatology and possible induced  
534 variability, *Journal of Atmospheric and Solar-Terrestrial Physics* 140, 23–33;  
535 <http://dx.doi.org/10.1016/j.jastp.2016.01.014>
- 536 Kramer, R., S. Wüst, C. Schmidt, and M. Bittner (2015). Gravity wave characteristics in the  
537 middle atmosphere during the CESAR campaign at Palma de Mallorca in 2011/2012: Impact  
538 of extratropical cyclones and cold fronts, *Journal of Atmospheric and Solar-Terrestrial*  
539 *Physics* 128 (2015) 8–23, <http://dx.doi.org/10.1016/j.jastp.2015.03.001>
- 540 Kai Ming Huang, Shao Dong Zhang, Fan Yi, (2010). Reflection and transmission of  
541 atmospheric gravity waves in a stably sheared horizontal wind field, *Journal of Geophysical*  
542 *Research: Atmospheres*, 10.1029/2009JD012687, **115**, D16,





- 543 Landès, M., Ceranna, L., Le Pichon, A., & Matoza, R. S. (2012). Localization of microbarom  
544 sources using the IMS infrasound network. *Journal of Geophysical Research:*  
545 *Atmospheres*, 117(D6).
- 546 Le Pichon, A., Cansi, Y. (2003). PMCC for infrasound data processing. *InfraMatics* 02, 1-9.
- 547 Le Pichon, A., Blanc, E., (2005). Probing high-altitude winds using infrasound. *J. Geophys.*  
548 *Res.*, 110, D20104. doi: 10.1029/2005JD006020
- 549 Le Pichon, A., Ceranna, L., Garcès, M., Drob, D., Millet, C., (2006). On using infrasound  
550 from interacting ocean swells for global continuous measurements of winds and temperature  
551 in the stratosphere. *J. Geophys. Res.*, 111, D11106. doi: 10.1029/2005JD006690  
552
- 553 Le Pichon, A., Vergoz, J., Blanc, E., Guilbert, J., Ceranna, L., Evers, L., Brachet, N., (2009).  
554 Assessing the performance of the International Monitoring System's infrasound network:  
555 Geographical coverage and temporal variabilities. *J. Geophys. Res.* 114, D08112. doi:  
556 10.1029/2008JD010907
- 557 Le Pichon, A., Ceranna, L., Vergoz, J. (2012). Incorporating numerical modelling into  
558 estimates of the detection capability of the IMS infrasound network. *J. Geophys. Res.*, 117,  
559 D05121. doi: 10.1029/2011JD016670  
560
- 561 Leovy, C. B., Sun, C. R., Hitchman, M. H., Remsberg, E. E., Russell III, J. M., Gordley, L.  
562 L., ... & Lyjak, L. V. (1985). Transport of ozone in the middle stratosphere: Evidence for  
563 planetary wave breaking. *Journal of Atmospheric Sciences*, 42(3), 230-244.  
564
- 565 Loyola D.G., Koukouli M.E., Valks P., Balis D.S., Hao N., van Roozendaal M., Spurr R.J.D.,  
566 Zimmer W., Kiemle S., Lerot C., Lambert J.-C. (2011) The GOME-2 total column ozone  
567 product: Retrieval algorithm and ground-based validation, *Journal of Geophysical Research*,  
568 vol. 116, D07302, Wiley-Blackwell
- 569 Marty, J., (2019). The IMS Infrasound Network: Current Status and Technological  
570 Developments, in: Le Pichon, A., Blanc, E., Hauchecorn, A. (Eds.), *Infrasound Monitoring*  
571 *for Atmospheric Studies. Challenges in Middle Atmosphere Dynamics and Societal Benefits.*  
572 Springer Nature Switzerland AG, pp. 3–62. doi:10.1007/978-3-319-75140-5\_1  
573



- 574 McIntyre, M. E., & Palmer, T. N. (1983). Breaking planetary waves in the stratosphere.  
575 *Nature*, 305(5935), 593-600.
- 576 Munro, R., Eisinger, M., Anderson, C., Callies, J., Corpaccioli, E., Lang, R., ... & Albinana,  
577 A. P. (2006, June). GOME-2 on MetOp. In Proc. of The 2006 EUMETSAT Meteorological  
578 Satellite Conference, Helsinki, Finland (Vol. 1216, p. 48).
- 579 Munro, R., et al. (2016): The GOME-2 instrument on the Metop series of satellites:  
580 instrument design, calibration, and level 1 data processing – an overview, *Atmos. Meas.*  
581 *Tech.*, 9, 1279–1301, <https://doi.org/10.5194/amt-9-1279-2016>.
- 582 Peters, D., Hoffmann, P., & Alpers, M. (2003). On the appearance of inertia-gravity waves on  
583 the north-easterly side of an anticyclone. *Meteorologische Zeitschrift*, 12(1), 25-35
- 584 Polvani, L. M., & Plumb, R. A. (1992). Rossby wave breaking, microbreaking, filamentation,  
585 and secondary vortex formation: The dynamics of a perturbed vortex. *Journal of Atmospheric*  
586 *Sciences*, 49(6), 462-476.
- 587 Pramitha, M., Venkat Ratnam, M., Taori, A., Krishna Murthy, B. V., Pallamraju, D., and  
588 Vijaya Bhaskar Rao, S. (2015). Evidence for tropospheric wind shear excitation of high-  
589 phase-speed gravity waves reaching the mesosphere using the ray-tracing technique, *Atmos.*  
590 *Chem. Phys.*, 15, 2709–2721, <https://doi.org/10.5194/acp-15-2709-2015>.
- 591 Rauthe, M., Gerding, M., Höffner, J., & Lübken, F. J. (2006). Lidar temperature  
592 measurements of gravity waves over Kühlungsborn (54° N) from 1 to 105 km: A winter-  
593 summer comparison. *Journal of Geophysical Research: Atmospheres*, 111(D24).  
594
- 595 Wüst, S., & Bittner, M. (2006). Non-linear resonant wave–wave interaction (triad): Case  
596 studies based on rocket data and first application to satellite data. *Journal of atmospheric and*  
597 *solar-terrestrial physics*, 68(9), 959-976.  
598
- 599 Wüst, S., Offenwanger, T., Schmidt, C., Bittner, M., Jacobi, C., Stober, G., Yee, J.H.,  
600 Mlynczak, M. G. & Russell III, J. M. (2018). Derivation of gravity wave intrinsic parameters  
601 and vertical wavelength using a single scanning OH (3-1) airglow spectrometer. *Atmospheric*  
602 *Measurement Techniques*, 11(5), 2937-2947.  
603



- 604 Smets, P.S.M., Evers, L.G. (2014). The life cycle of a sudden stratospheric warming from  
605 infrasonic ambient noise observations, *J. Geophys. Res. Atmos.*, 119, 12,084-12,099
- 606 Spurr, R., Loyola, D., Heue, K. P., Van Roozendaal, M., & Lerot, C. (2022). S5P/TROPOMI  
607 Total Ozone ATBD. Deutsches Zentrum für Luft- und Raumfahrt (German Aerospace  
608 Center), Weßling, Germany, Tech. Rep. S5P-L2-DLR-ATBD-400A.
- 609 Szuberla, C.A.L., Olson, J.V., (2004). Uncertainties associated with parameter estimation in  
610 atmospheric infrasound rays. *J. Acoust. Soc. Am.* 115, 253-258. doi: 10.1121/1.1635407
- 611 Veefkind, J. P., Aben, I., McMullan, K., Förster, H., De Vries, J., Otter, G., ... & Levelt, P. F.  
612 (2012). TROPOMI on the ESA Sentinel-5 Precursor: A GMES mission for global  
613 observations of the atmospheric composition for climate, air quality and ozone layer  
614 applications. *Remote sensing of environment*, 120, 70-83.
- 615
- 616